Energy & Environmental Science

ROYAL SOCIETY OF CHEMISTRY

PAPER

View Article Online
View Journal | View Issue

Cite this: *Energy Environ. Sci.*, 2025, **18**, 8667

Engineering an ion-pumping solid electrolyte interphase for ultra-stable aqueous zinc-ion batteries under deep discharge conditions

Leixin Yang,†*[ab] Yujie Shen,†[a] Xintao Long,†[c] Qianyi Ma,[d] Ziqing Ruan,[a] Nuo Xu,[a] Kaihua Li,[a] Long Jiao,[a] Yaping Kong,[e] Jie Li,[a] Lei Tang,*[f] Aiping Yu *[d] and Bowen Cheng*[a]

Received 11th March 2025,
Accepted 25th July 2025

DOI: 10.1039/d5ee01408e

rsc.li/ees

Meeting global terawatt-scale energy demands necessitates innovative solutions to overcome the critical challenges faced by aqueous Zn-ion batteries, particularly the poor reversibility and unstable plating/stripping of Zn anodes under high depths of discharge (DOD). In this work, we introduce a novel composite artificial solid electrolyte interphase (SEI), termed P–G, which combines a poly(ether-*block*-amide) matrix with graphene oxide (GO). By leveraging the functional groups of the polymer (C=O, C–O–C) and the electronegativity of GO, the P–G SEI layer can act as a highly efficient Zn^{2+} ion pump, achieving a remarkable Zn^{2+} transference number of 0.77 and fast ion transport kinetics. Comprehensive theoretical and experimental analyses demonstrate that the P–G SEI layer regulates Zn^{2+} coordination and forms rapid ion transport pathways, leading to a highly stable and reversible Zn anode. As a result, P–G@Zn symmetric cells achieved ultra-stable cycling for 6500 h at 1 mA cm^{-2} and a record-breaking lifespan exceeding 5000 h at 54.7% DOD. Furthermore, a high-specific-energy P–G@Zn||I_2 pouch cell delivered exceptional performance, retaining 82.8% capacity after 400 cycles with an N/P ratio of 2. This study offers a compelling framework for designing an advanced composite SEI layer, paving the way for highly reversible Zn-ion batteries in practical energy storage applications.

Broader context

The urgent need for sustainable, high-performance energy storage solutions drives innovation in aqueous zinc-ion batteries (AZIBs), which offer safety and scalability for grid applications. However, Zn anode instability, caused by dendrite growth and parasitic reactions, limits their practical viability under high-depth cycling. A graphene oxide-reinforced poly(ether-*block*-amide) artificial solid electrolyte interphase (SEI) (P–G) is introduced that synergistically combines polymer functional groups and the electronegativity of GO to direct Zn^{2+} flux and suppress dendrites. As a result, P–G@Zn symmetric cells exhibit a record-breaking lifespan exceeding 5000 h at 54.7% depths of discharge (DOD) and ultra-stable cycling for 6500 h at 1 mA cm^{-2}. The P–G layer achieves a high Zn^{2+} transfer number (0.77) and rapid ion kinetics, enabling reversible Zn deposition. Additionally, a high-specific-energy P–G@Zn||I_2 pouch cell retains 82.8% capacity after 400 cycles with an N/P ratio of 2, validating practical feasibility. By integrating experimental and theoretical insights, this work bridges innovations developed in laboratory settings and practical AZIB deployment, establishing a universal framework for stabilizing metal anodes in next-generation batteries.

[a] *State Key Laboratory of Bio-based Fiber Materials, Tianjin Key Laboratory of Pulp and Paper, China Textile Industry Key Laboratory of High-performance Fibers Wet-laid Nonwoven Materials, Tianjin University of Science and Technology, Tianjin 300457, China. E-mail: Leixinyang@tust.edu.cn, bowenc17@tust.edu.cn*
[b] *Wanli Energy Technology Development Co., Ltd., Institute of Carbon Neutrality, Zhejiang Wanli University, Ningbo 315100, China*
[c] *Guangdong Provincial Key Laboratory of Nanophotonic Functional Materials and Devices, School of Information and Optoelectronic Science and Engineering, South China Normal University, Guangzhou 510006, China*
[d] *Department of Chemical Engineering, Waterloo Institute for Nanotechnology, University of Waterloo, Waterloo, ON, N2L3G1, Canada. E-mail: aipingyu@uwaterloo.ca*
[e] *Vacuum Interconnected Nanotech Workstation, SINANO, CAS, Suzhou 215123, China*
[f] *Institute of Sustainability for Chemicals, Energy and Environment (ISCE2), Agency for Science, Technology and Research (A*STAR), 1 Pesek Road, Singapore 627833, Republic of Singapore. E-mail: Tang_Lei@isce2.a-star.edu.sg*
† Leixin Yang, Yujie Shen, and Xintao Long contributed equally to this work.

Introduction

The increasing global demand for sustainable energy and great interest in environmental stewardship have driven the intense research of next-generation electrical energy storage (EES) systems powered by renewable and clean energy sources.[1,2] Among these, aqueous zinc-ion batteries (AZIBs) are a promising solution for grid-scale energy storage due to their high theoretical capacity (820 mAh g^{-1} or 5854 mAh cm^{-3}), low redox potential (−0.76 V *vs.* SHE), intrinsic safety, and low cost. However, despite these advantages, the widespread adoption of AZIBs has been hindered by critical challenges associated with the reversibility and stability of zinc (Zn) metal anodes, particularly under high depths of discharge (DOD). Issues such as the hydrogen evolution reaction (HER), corrosion, and dendrite formation lead to low coulombic efficiency and poor cycle life,[3–5] primarily due to the thermodynamic instability of Zn metal in neutral or mildly acidic electrolytes.[6–8]

A fundamental limitation of AZIBs compared to lithium-ion batteries (LIBs) is their inability to naturally form a robust solid electrolyte interphase (SEI) layer, which is crucial for mitigating challenges.[9] To overcome these barriers, researchers have explored a range of strategies, including advanced electrode structure designs, electrolyte optimization, separator modifications, and protective layer engineering.[10–12] Among these approaches, constructing protective layers is particularly promising because it enables the direct formation of functional SEI layers on Zn anodes *via in situ* generation or *ex situ* coating.[13] Polymer-based artificial SEI layers are especially attractive due to their excellent interfacial affinity and tunable functional groups. However, achieving mechanically and chemically stable polymer layers in aqueous environments remains difficult, as they must also adequately minimize interfacial resistance and maintain efficient ion transport.

In this regard, two-dimensional (2D) materials have emerged as transformative components in protective coatings. Because of their atomic-scale thickness, exceptional mechanical strength, and unique electrochemical properties, they are ideal for addressing the limitations of Zn anodes. Recent studies combining polymers with 2D materials have demonstrated significant progress in enhancing cycling stability.[14–16] For example, hybrid layers incorporating 2D $Ti_3C_2T_x$ nanosheets or 2D metal–organic frameworks have shown excellent reversibility and improved Zn^{2+} transport.[17] Despite these breakthroughs, current solutions are mainly effective at low DOD (below 50%), because the Zn anode undergoes more severe structural degradation and side reactions under high DOD. Therefore, developing SEI coatings that enable uniform electric field distribution and stable Zn^{2+} plating/stripping at high DOD is essential, but it is highly challenging for AZIBs to be used in large-scale applications.[18,19]

Drawing inspiration from biological ion pumps—such as ATPase proteins that mediate Na^+/K^+ transport across cell membranes by leveraging coordination interactions to drive active ion movement against concentration gradients—we introduce a biomimetic 'ion-pumping' concept for advanced solid electrolyte interphase design.[20] In this work, we address this by designing a hybrid SEI layer (P–G) comprising a poly(ether-*block*-amide) polymer and graphene oxide (GO), forming a hydrogen-bond-linked network with an ion-pumping effect (Fig. 1a). The P–G SEI layer enhances bonding strength and facilitates rapid Zn^{2+} transport on the Zn surface (P–G@Zn). The electronegativity of GO induces selective Zn^{2+} transport, enabling uniform, dendrite-free Zn deposition. The functional groups (C═O, C–O–C) of the P–G SEI layer regulate the Zn^{2+} solvation structure and electrolyte concentration, suppressing the HER and byproduct formation. As a result, the P–G SEI layer achieves exceptional electrochemical performance.

Symmetrical cells exhibit an ultra-long lifespan of 6500 h at 1 mA cm^{-2}, and stable cycling over 5000 h at 54.7% DOD. Additionally, Zn||I_2 full cells show superior capacity retention of 95.5% over 36 000 cycles, and excellent cycling stability in pouch cells at high specific energy and Zn DOD. This work offers new insights into designing advanced SEI layers, paving the way for the practical application of AZIBs in next-generation energy storage systems.

Results and discussion

Construction and characterization of P–G

Graphene oxide (GO), a prominent two-dimensional material, is known for its excellent conductivity, an ultrahigh specific surface area, and superior mechanical strength.[21] Because of these properties, it is a suitable candidate for dispersing current density, restricting lateral diffusion of Zn^{2+}, and promoting uniform deposition. The foundational characteristics of the GO employed throughout this work are summarized in Table S1, with corresponding experimental testing protocols detailed in Fig. S1 and S2. However, when applied as an SEI layer for zinc anodes, GO binds weakly with zinc primarily through van der Waals forces between layers, resulting in poor structural stability. Consequently, GO tends to restack on the surface, and thus, complete coverage is difficult (Fig. S3). Additionally, as shown in Fig. S4, GO tends to peel off during the bending of zinc foil.

To address these limitations, poly(ether-*block*-amide) (PEBA) was chosen to enhance the bonding between the SEI layer and zinc metal. PEBA, a multifunctional polymer, was dissolved in a homogeneous solution, blended with GO, and drop-cast onto a zinc foil surface (Fig. S5).[22] The drop-casting method is advantageous compared to other preparation methods because of its simplicity and low cost. The structure of PEBA includes hydrophilic C–O–C groups in the PEO chain segment and zincophilic –CO–NH– groups in the PA chain segment (Fig. S6), contributing to its multifunctionality.[23]

The composite material, termed P–G, was characterized using Fourier transform infrared (FTIR) spectroscopy. As shown in Fig. 1b and Fig. S7, GO exhibits a peak at 1640 cm^{-1}, which was attributed to the stretching vibration of C═O in carboxyl groups, and a broad peak is observed at 3300 cm^{-1},

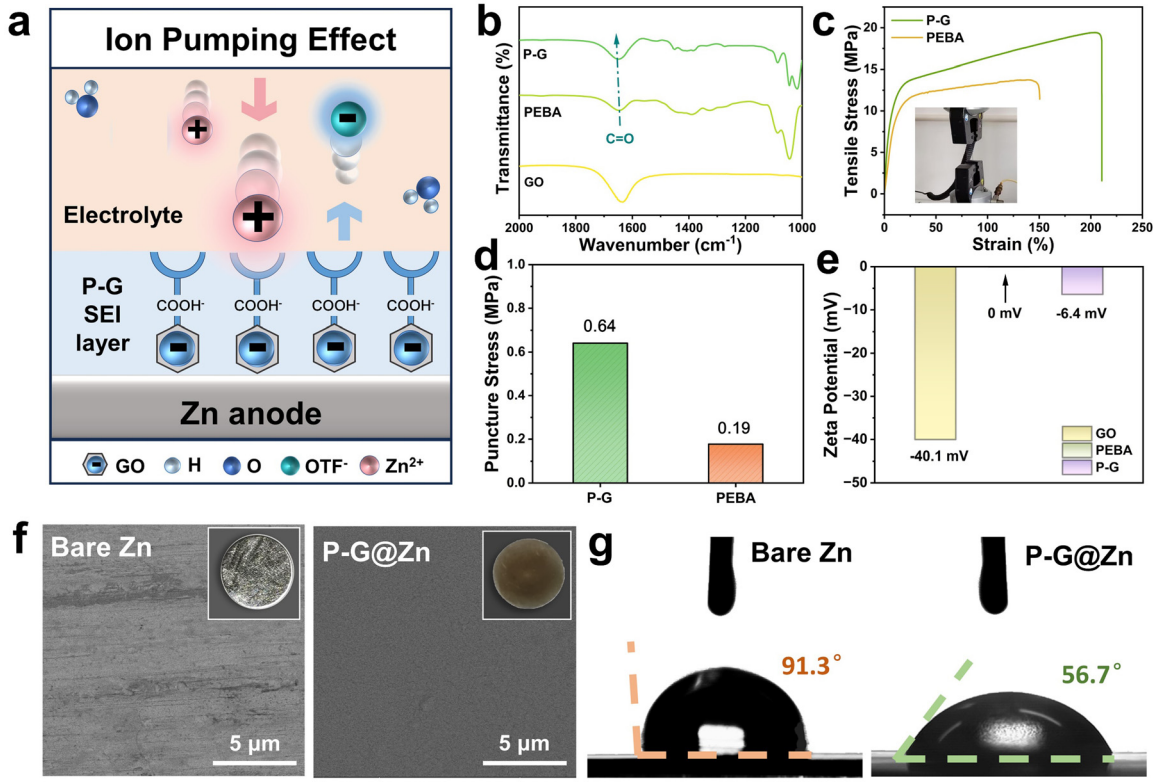

Fig. 1 Structural characterizations of the P–G SEI layer. (a) A schematic diagram of the regulating mechanism of the ion pump in the P–G SEI layer. (b) Partial magnification of the FTIR spectra of GO, PEBA, and P–G. (c) Elongation at break of PEBA and P–G films after drying. (d) Mechanical properties of PEBA and P–G films. (e) Zeta potential of GO, PEBA, and P–G. (f) Optical images and SEM images of bare Zn foil and P–G@Zn foil. (g) Contact angles of 3 M OTF aqueous solution on bare Zn foil and P–G@Zn foil.

corresponding to O–H vibrations. PEBA displays characteristic peaks related to N–C═O and –O– groups.[24] In the P–G SEI layer, the presence of both types of characteristic peaks, along with shifts in the C═O peak, confirmed the formation of hydrogen bonds between GO and PEBA.

Mechanical testing further highlighted the advantages of the composite material. Films of PEBA and P–G were prepared on a PTFE substrate *via* tape casting and were then subjected to tensile tests (Fig. 1c). The PEBA film demonstrated excellent mechanical strength due to the rigid PEO segments, while the addition of hydrogen bonds in the composite film significantly enhanced its performance, allowing it to withstand tensile forces of nearly 20 MPa. Remarkably, the P–G film exhibited exceptional flexibility in wet environments, with an elongation at break exceeding 1100% (Fig. S8). Additionally, the puncture resistance of the P–G SEI layer was three times that of pure PEBA film (Fig. S9). These characteristics ensured sufficient mechanical properties to accommodate volume changes and resist dendritic punctures during zinc plating/stripping cycles (Fig. 1d).

To optimize the P–G SEI layer's thickness and polarization voltage, the amount of drop-coating solution was varied, with 45 μL yielding the most optimal electrical performance and cycle life (Fig. S10). As shown in Fig. S11, systematic modulation of the GO concentration revealed a direct correlation with electrochemical performance, where the optimized loading of 1.0 mg cm^{-2} delivered superior cycling stability. Zeta potential measurements showed that the surface potential of GO is −40.1 mV (Fig. 1e), which is primarily due to its abundant oxygen-containing functional groups, such as carboxyl (–COOH) and hydroxyl (–OH). The negatively charged GO imparts electronegativity to the P–G surface, thereby enhancing its attraction to Zn^{2+} ions while repelling anions.[25]

Scanning electron microscopy (SEM) images (Fig. 1f) reveal a dense and uniform 10-μm-thick protective layer on the zinc surface, where nano-sized GO is tightly anchored in the PEBA matrix. Energy-dispersive spectroscopy (EDS) analysis (Fig. S13) confirmed the uniform distribution of C and O elements on the surface, with no visible zinc underneath, indicating complete coverage. Even after repeated folding of the zinc foil, the protective layer remained intact, highlighting its durability and efficacy in long-term cycling (Fig. S15).

Contact angle measurements using a 3 M $Zn(OTf)_2$ electrolyte were performed to evaluate the wettability of the protective layer. Compared to a contact angle of 91.3° on bare zinc, the P–G SEI layer exhibited a significantly lower angle of 56.7° (Fig. 1g), suggesting enhanced wettability. This improved wettability can be attributed to the abundant hydroxyl groups and ether oxygen bonds in the P–G SEI layer, which also enhance the solvation structure of Zn^{2+} and facilitate the diffusion of water molecules on the surface, further supporting its role in stabilizing zinc anodes.[19]

Characterization of anti-corrosion capability

Continuous interface corrosion between the electrode and electrolyte in assembled cells leads to the formation of byproducts and the HER, significantly limiting the performance of AZIBs.[26] To evaluate the corrosion resistance of the P–G SEI layer, zinc plates with and without coatings were immersed in electrolytes. As shown in Fig. 2a, after five days of soaking, the surface of the bare zinc plate exhibited large dendrites and blocky byproducts, as revealed by SEM images. In contrast, the zinc plate with the P–G SEI layer showed minimal corrosion after the coating was removed.

XRD analysis of the surface-passivated zinc foil revealed distinct peaks at 6.6°, 13.1°, 19.8°, and 31.2°, indicating corrosion on the zinc surface in the absence of P–G protection and decomposition of $(OTf)^-$ anions (Fig. 2b). This demonstrates that the protective layer effectively prevents corrosion. Additional SEM observations (Fig. S16) revealed that the P–G SEI layer formed a flawless coating on the zinc plate that maintained excellent corrosion protection even after 14 days of electrolyte immersion, as evidenced by the absence of dendrites and significant byproduct peaks (Fig. S17).

To assess the thermodynamic stability of the P–G SEI layer, corrosion current density measurements were performed. As shown in Fig. 2c, the corrosion current density of bare zinc in the electrolyte was 19.6 mA cm^{-2}, which is significantly higher than that of P–G@Zn (5.1 mA cm^{-2}). Moreover, the coated zinc foil exhibited an increase in corrosion potential, indicating an enhanced anti-corrosion performance. These results demonstrate the positive effect of the P–G SEI layer in improving the corrosion resistance of the zinc metal anode.

The effectiveness of the P–G SEI layer in suppressing the HER was evaluated through linear sweep voltammetry (LSV) in a three-electrode system. To avoid interference from zinc deposition, 1 M Na_2SO_4 was used as the electrolyte. In this setup, the zinc foil served as the working electrode, the Pt foil as the counter electrode, and Ag/AgCl as the reference electrode.[27] As shown in Fig. 2d, the P–G SEI layer reduced the cathodic current density from 42.0 mA cm^{-2} to 28.7 mA cm^{-2}, accompanied by a larger polarization potential. Optical images revealed a significant number of bubbles on the bare zinc anode surface during the test, whereas no bubbles were observed on the P–G SEI layer surface. This directly confirms that the protective layer suppressed the HER and was

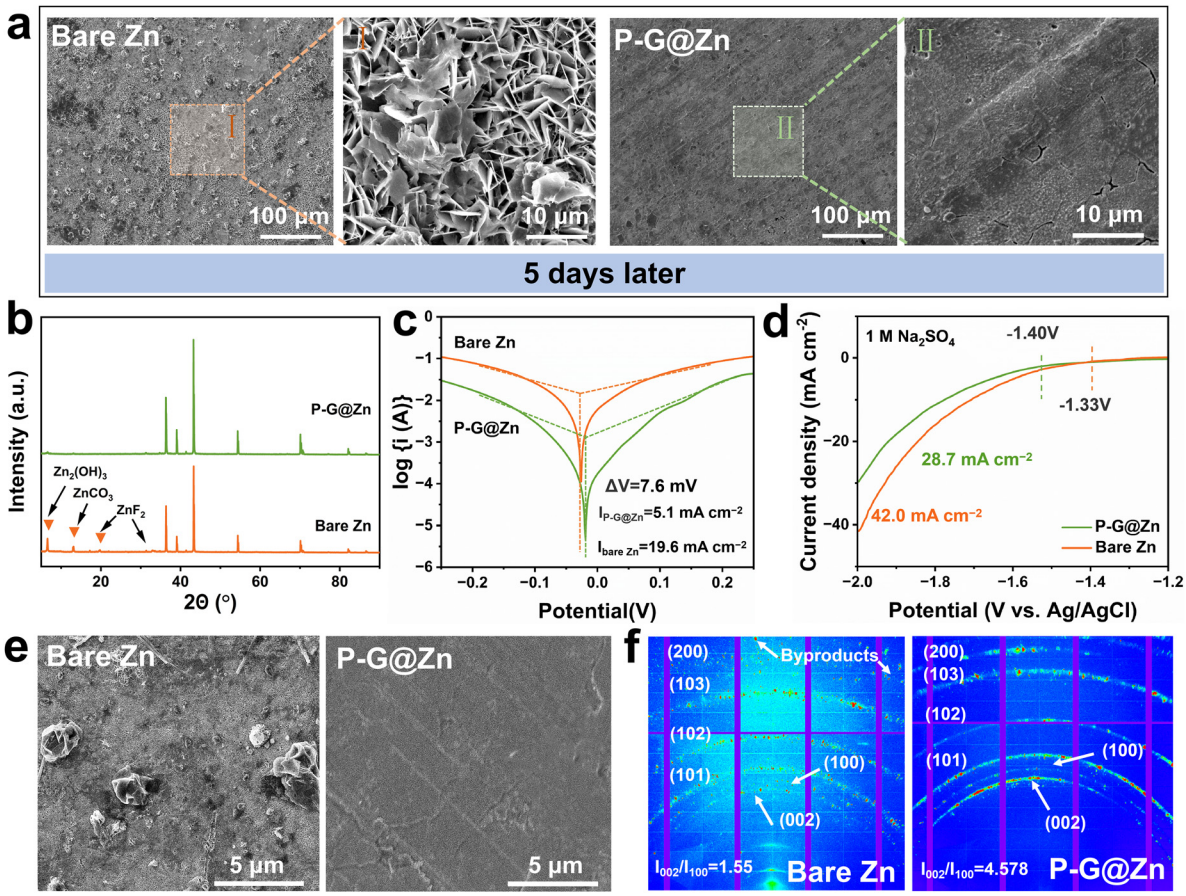

Fig. 2 Anti-corrosion performance of the P–G@Zn anode. (a) Surface SEM images of bare Zn and P–G@Zn immersed in electrolyte after 5 days. (b) XRD patterns of bare Zn and P–G@Zn soaked in electrolyte after 5 days. (c) Tafel curves of bare Zn and P–G@Zn. (d) LSV curves of bare Zn and P–G@Zn. (e) SEM images of bare Zn and P–G@Zn after removing the P–G layer after cycling 60 h at 1 mA cm^{-2}. (f) WAXS patterns for cycled bare Zn and cycled P–G@Zn.

consistent with the test data (Fig. S20). A lower corrosion current density and more positive corrosion potential typically signify superior corrosion resistance.[28]

The excellent corrosion resistance of the P–G SEI layer contributed to a dendrite-free anode during cycling. To further investigate this, symmetrical cells were cycled at 1 mA cm^{-2} (1 mAh cm^{-2}) for 30 cycles. While dendritic structures were observed on the bare zinc anode after cycling, the P–G@Zn|| P–G@Zn cell exhibited a smooth anode surface (Fig. 2e). The XRD patterns of the uncoated and coated anodes revealed differences in the peak intensity ratio of the (002) plane to the (100) plane (Fig. S21). The ratio for the P–G@Zn anode was 4.578, which was significantly higher than 1.55 observed for the bare Zn anode. The dominance of the Zn (002) plane, characterized by lower surface energy and higher stability, supports uniform horizontal deposition of zinc ions and inhibits dendrite formation.

Further insights into crystal structure changes after cycling were obtained using two-dimensional wide-angle X-ray scattering (WAXS) patterns (Fig. 2f). The bare zinc anode displayed chaotic diffraction peaks and significant byproduct diffraction peaks, which were nearly absent on the P–G SEI layer.[29] This indicates that the zinc deposits on the bare surface were random and irregular, leading to severe tip discharge effects and exacerbated dendrite growth.[30] The P–G SEI layer demonstrated excellent thermodynamic and kinetic stability. Its superior wettability captured water molecules and homogenized the surface electrolyte, effectively shielding the zinc anode from direct contact with the electrolyte. As a result, the P–G SEI layer prevented corrosion, suppressed the HER, and minimized byproduct formation, ensuring long-term stability and performance for AZIBs.

Characterization of deposition behavior

To investigate the influence of the ion pump effect from the P–G SEI layer on zinc deposition behavior, chronoamperometry (CA) was conducted to analyze the zinc ion growth mechanism on the anode (Fig. 3a). The current variation was monitored over 150 seconds under a constant potential of 150 mV. For the bare zinc electrode, the current density continuously increased, indicating rampant 2D diffusion on the anode surface. This uncontrolled diffusion leads to uneven zinc deposition, where the severe tip effect promotes dendritic growth. Such dendrites can puncture the separator, potentially causing battery short circuits.[31] In contrast, with the P–G SEI layer, the current curve stabilized within 30 seconds and ceased decreasing, suggesting that the system quickly transitioned to stable three-dimensional (3D) diffusion. This behavior enables uniform zinc ion deposition on the anode surface, ultimately forming Zn^0.[32]

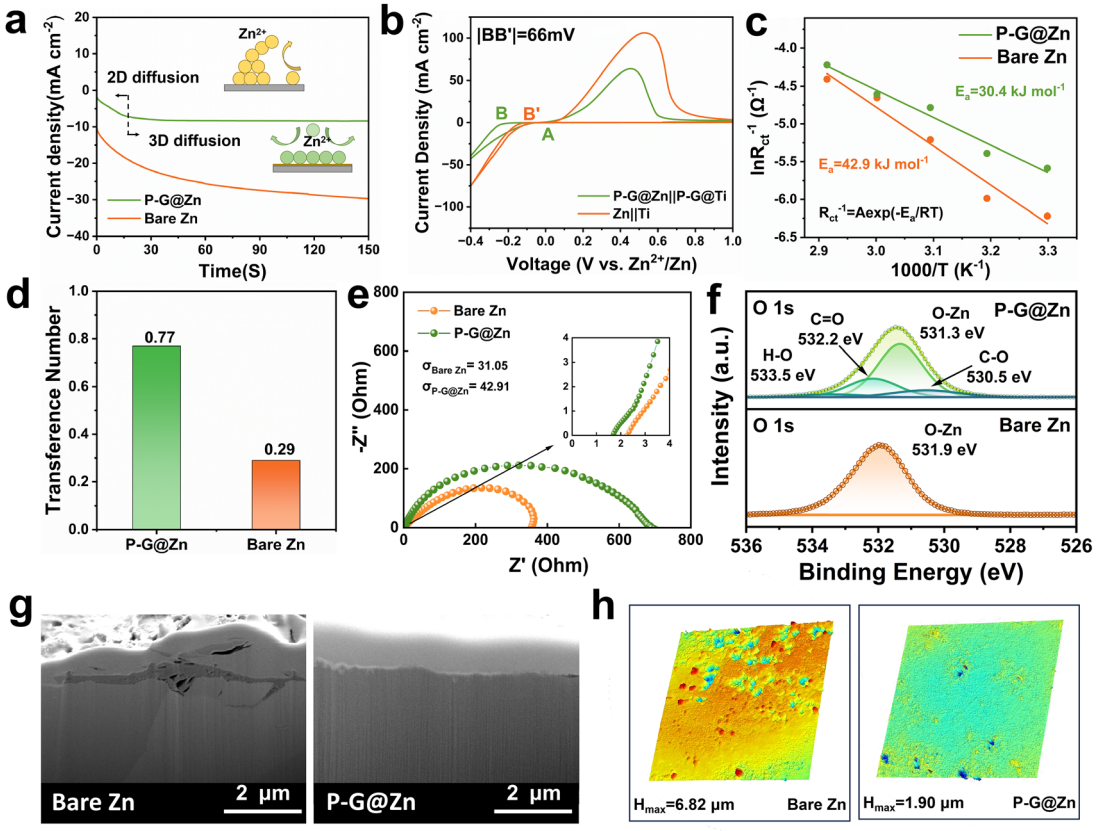

Fig. 3 Regulation of the Zn^{2+} deposition behavior of the P–G SEI layer. (a) CA curves at −150 mV overpotential. (b) CV curves. (c) Arrhenius curves. (d) Zn^{2+} transference numbers of bare Zn and P–G@Zn symmetric cells. (e) Ionic conductivity (unit: mS cm^{-1}). (f) XPS spectra of O 1s. (g) Cross-section SEM images of cycled anodes post FIB etching. (h) Surface roughness of cycled anodes after 30 cycles (1 mA cm^{-2}, 1 mAh cm^{-2}).

In addition, a zinc–copper cell was constructed, and the nucleation potential of zinc was assessed through cyclic voltammetry (CV) testing, as depicted in Fig. 3b. The uniform deposition of Zn^{2+} was largely attributed to the initial nucleation behavior. Point A represents the potential intersection of the CV curves, while point B/B′ indicates the onset of zinc ion reduction on the copper anode surface. The potential difference between these points, termed the nucleation overpotential, is a critical factor. On the P–G SEI layer surface, the presence of abundant polar groups with strong coordination capabilities prevents uncontrolled zinc ion diffusion and increases the deposition potential. This is reflected in the CV results, where the nucleation overpotential of P–G@Zn is higher than that of the bare zinc–copper cell (66 mV).[33] Notably, although the nucleation overpotential of the coated anode was higher than that of the control, classical nucleation theory suggests that this promotes a higher nucleation site density, leading to more uniform Zn deposition with finer particle size. The increased overpotential also provides a stronger thermodynamic driving force for the formation and growth of finer Zn nuclei.

The ion pump effect of the P–G SEI layer facilitates Zn^{2+} transport, expediting zinc deposition. With this mechanism, a stable potential difference is maintained on the electrode surface, preventing random migration and aggregation of zinc ions and ensuring uniform deposition. As shown in Fig. S22, the morphology of zinc deposited on the copper surface at a current density of 0.5 mA cm^{-2} reveals a porous zinc coating in the bare Zn||Cu semi-symmetric cell. In contrast, the P–G SEI layer exhibits a denser galvanized layer. Similarly, Fig. S23 highlights significant differences in the zinc anode surfaces, further demonstrating their impact.

The nucleation behavior of zinc ions can also be modulated by regulating the solvation structure of Zn^{2+} through the protective layer. During the electroplating process, Zn^{2+} must overcome the desolvation energy barrier from $[Zn(H_2O)_6]^{2+}$.[34] A high energy barrier slows zinc ion migration, leading to significant concentration and potential differences between the zinc anode and electrolyte, which adversely affect battery reversibility.[35] As shown in Fig. S24, the charge transfer resistance (R_{ct}) of Zn@P–G is lower than that of a bare Zn cell at the same temperature, indicating enhanced anode migration kinetics after coating.[3]

The FTIR results (Fig. S25 and S26) reveal a redshift in the characteristic bands of C–O–C and C═O, confirming chemical interactions between Zn^{2+} and the P–G SEI layer. The activation energy (E_a) was obtained using the Arrhenius equation to investigate and evaluate the desolvation capability of the zinc anode with and without P–G. Fig. 3c illustrates that the P–G@Zn anode reveals a smaller E_a of 30.4 kJ mol^{-1} in comparison with the bare Zn anode (42.9 kJ mol^{-1}). This demonstrates that the P–G SEI layer can accelerate the Zn^{2+} desolvation process and facilitate ion migration kinetics.

The uniform and dense P–G SEI layer also facilitates the dissociation of water molecules in hydrated zinc ions. The Zn-ion transference number ($t_{Zn^{2+}}$) was measured to evaluate the migration speed of zinc ions (Fig. 3d and Fig. S27). Compared with the initial interfacial resistance of bare zinc, the initial interfacial resistance of P–G@Zn increased to a certain extent due to the introduction of the polymer coating. It was observed that the increase in the resistance of bare zinc was significantly higher compared to the resistance exhibited by the P–G SEI layer. Calculations showed that the $t_{Zn^{2+}}$ values for bare zinc and P–G@Zn are 0.29 and 0.77, respectively. It is worth noting that although the Zn^{2+} transference number reflects the bulk properties of the electrolyte, the anode coating can indirectly influence the measured value by: (i) inhibiting side reactions that alter the bulk composition; (ii) stabilizing the electrode–electrolyte interface; and (iii) affecting the interfacial concentration profile and polarization behavior involved in the measurement process.

As shown in Fig. 3e, it was found that ionic conductivity of approximately 42.91 mS cm^{-1} was achieved for P–G@Zn, which represents the total impedance of the cell and indicates the effective conductivity of the full interfacial configuration. The ionic conductivity of the free-standing P–G SEI layer was measured at 31.05 mS cm^{-1} (Fig. S28), which indicates that the construction of the P–G SEI layer serves as an effective strategy to enhance the migration rate of zinc ions at the P–G@Zn interface. These findings demonstrate that the P–G SEI layer effectively enhances the zinc-ion migration rate.

X-ray photoelectron spectroscopy (XPS) and focused ion beam scanning electron microscopy (FIB-SEM) analyses were conducted to investigate the surface reactions and morphology of the zinc anode after cycling.[36,37] As shown in Fig. 3f and Fig. S29, the O 1s peaks at 532.2 eV and 530.5 eV correspond to C–O and C═O bonds, respectively, while the N 1s peak at 398.2 eV, attributed to N–Zn bonds, is absent in the bare zinc electrode. This finding indicates that the artificial SEI participates in Zn^{2+} desolvation and effectively regulates its diffusion behavior.[38]

FIB-SEM images reveal significant surface irregularities and inconsistent zinc deposition with voids and cracks on the cycled bare Zn, whereas the removal of the P–G SEI layer exposes a uniform and void-free zinc surface (Fig. 3g and Fig. S30). The 3D reconstruction images (Fig. 3h) further show that the maximum surface height of cycled Zn (6.82 μm) is three times greater than that of P–G@Zn (1.90 μm), with the latter exhibiting a much smoother surface, as indicated by the surface roughness analysis.[39] These results demonstrate that the P–G SEI layer provides abundant adsorption sites for zinc ions and nano-ion channels, which are anticipated to significantly enhance the cycling performance of AZIBs.

Mechanisms of the P–G SEI layer in regulating Zn deposition

Issues such as dendrite formation and side reactions observed on the bare zinc anode were effectively mitigated by the artificial SEI layer through multiple protective mechanisms (Fig. 4a). On the rough and defective surface of the bare zinc anode, uneven Zn^{2+} concentration distribution between the electrolyte and metal surface led to random deposition of Zn^{2+} at regions with high tip potential, triggering the tip effect.[40] This resulted in dendrite formation and 'dead zinc,'

which negatively impacts the cycle performance of AZIBs. Additionally, the desolvation process releases H_2O, which undergoes the HER on the metal surface, releasing H^+ ions and altering the cell's pH. This, in turn, initiates corrosion and generates byproducts that further disturb the electric field distribution, increasing cell impedance.[41]

The P–G SEI layer, with its excellent surface wettability and abundant functional groups, accelerates the dissolution process of Zn^{2+}. Critically, this induces an 'ion pump effect' driven by the strong coordination affinity between the artificial SEI layer and Zn^{2+}, enabling their active transport against concentration gradients and promoting directional acceleration at the anode interface. The uniformly distributed GO on the zinc surface forms ion transport channels, facilitating the rapid *in situ* deposition of Zn^{2+}.[42,43]

The adsorption behavior of Zn^{2+} at various sites on the anode surface can be further investigated to elucidate Zn^{2+} migration kinetics using density functional theory (DFT) simulations (Fig. 4b).[44,45] The binding energy of Zn^{2+}–$6H_2O$ is significantly weaker than the adsorption strength of Zn^{2+} at various active sites in the P–G SEI layer, as shown in Fig. S31 and S32. In particular, the binding energy of the Zn^{2+}–O atom (−1.38 eV) in GO (C═OOH) is the highest, confirming that the ion pump effect in the P–G SEI layer facilitates the desolvation process of Zn^{2+} and guides uniform Zn^{2+} flux. For the sake of comparing the difference in Zn^{2+} surface concentration distribution caused by Zn dendrite growth with or without the P–G SEI layer, modelling and finite element analysis were carried out using COMSOL software (Fig. S33).[37,46] As illustrated in Fig. 4c and Fig. S34, while Zn^{2+} accumulates at dendritic sites on bare Zn, the P–G SEI layer demonstrates homogeneous Zn^{2+} deposition *via* directional ion pumping.

X-ray absorption fine structure (XAFS) analysis was utilized to simulate the Zn^{2+} solvation structure on the P–G SEI layer surface and in 3 M OTF electrolyte. In the X-ray absorption near edge structure (XANES) spectra, zinc foil exhibited the lowest leading edge peak energy, indicative of Zn^0 (Fig. 4d).[47] In contrast, P–G/OTF demonstrated a moderate edge peak energy, suggesting that the valence state of Zn in the P–G SEI layer is lower than that in the OTF electrolyte.[48] The shift of the absorption edge towards a lower energy indicates an increased electron density surrounding Zn^{2+}. This alteration in valence

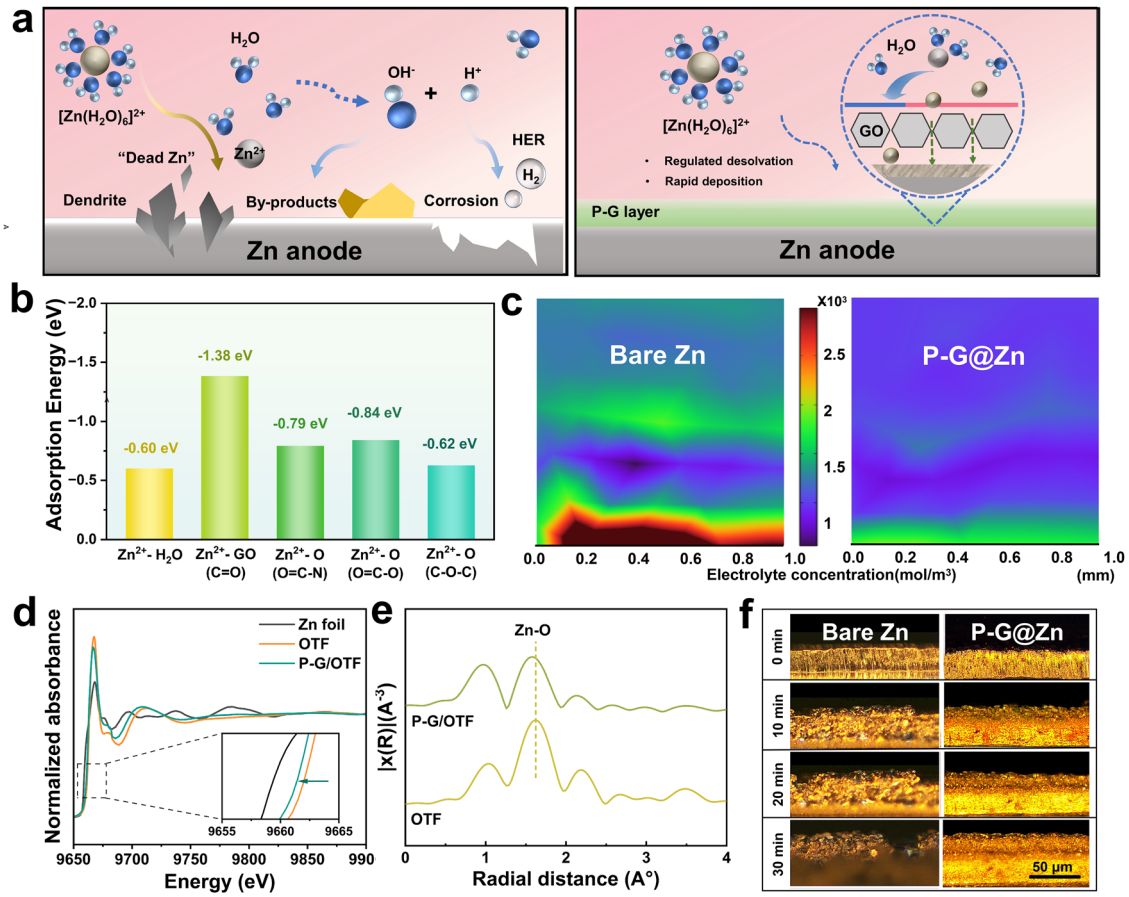

Fig. 4 Mechanisms used by the P–G SEI layer in regulating Zn deposition. (a) Schematic diagram illustrating the effect of the P–G SEI layer in the highly reversible zinc anodes. (b) Corresponding binding energies of Zn^{2+} with different ligands. (c) Simulation results of electrolyte concentration distribution on bare Zn and the P–G@Zn surface. (d) Zn K-edge XANES spectra of Zn foil, OTF electrolyte, and P–G/OTF electrolyte. (e) Fourier transform extended X-ray absorption fine structure (FT-EXAFS) in *R* space. (f) *In situ* microscopic images of bare Zn and the P–G@Zn surface following 0, 10, 20, and 30 min treatments at 10 mA cm^{-2}.

state arises from the negatively charged GO in the P–G SEI layer acting as an electron donor, and thereby modulating the solvation structure of Zn^{2+}.

As illustrated in Fig. 4e, the predominant single-coordination shell at approximately 1.8 Å was attributed to Zn–O interactions, while the peak observed near 1 Å resulted from low-frequency noise generated during testing. The presence of the P–G SEI layer led to a reduction in the radial distance of Zn-O (from 1.63 Å to 1.59 Å), indicating an enhanced interaction between the P–G SEI layer and Zn^{2+}. This modification facilitates the dissolution of Zn^{2+} at the electrode–electrolyte interface during deposition.[49,50]

The findings demonstrate that the P–G SEI layer effectively optimizes the solvation structure of Zn^{2+}. To visualize the deposition process of Zn^{2+}, we monitored the deposition of Zn^{2+} using an *in situ* optical microscope under high current conditions of 10 mA cm^{-2}. Within 30 minutes, large and uneven zinc deposits appeared on the surface of the bare Zn, accompanied by the formation of visible grey byproducts and bubbles. On the contrary, on the surface of P–G@Zn, Zn^{2+} was deposited more finely and uniformly (Fig. 4f). In addition, the nanoindentation test was conducted to analyze the formation of dendrite anodes from a physical perspective (Fig. S35). The P–G SEI layer shows a low hardness and small elastic modulus (E_r) value of 0.33 GPa, which is significantly smaller than the cycled P–G@Zn anode (with the P–G SEI layer removed) of 24.1 GPa. This phenomenon was mainly attributed to the fact that the P–G layer facilitates the formation of a dendrite-free anode by ensuring a uniform zinc ion flux, instead of suppressing dendrite formation through a physical mechanism.

Electrochemical stability and reversibility of the Zn electrodes

The plating/stripping performance of the zinc anode was evaluated through a constant current long-term cycle of symmetrical and asymmetric cells.[51–53] At a current density of 1 mA cm^{-2}, bare Zn||Zn symmetric cells experienced short circuits after just 140 h, likely due to the hydrogen evolution reaction (HER) and uncontrolled dendrite growth (Fig. 5a). In contrast, P–G@Zn||P–G@Zn cells exhibited remarkable electrochemical performance, maintaining stable cycling for up to 6600 h. Post-cycling analysis revealed a significant increase in the thickness of the bare Zn cell, which was attributed to the HER during electrolyte immersion, leading to anode degradation and electrolyte consumption (Fig. S36). It is worth noting that the polarization voltage of the P–G@Zn cell remained stable for over 6000 h, even as the current density increased from 1 to 20 mA cm^{-2}. This indicates the P–G SEI layer's adaptability to high currents and its durability under fast charging and discharging conditions. In contrast, bare Zn symmetric cells showed irregular polarization curves and rapid deactivation at higher current densities (Fig. 5b).

Coulombic efficiency (CE), a critical parameter for evaluating electrode reversibility, is determined by the ratio of zinc stripped and deposited during a cell cycle.[54,55] In addition to

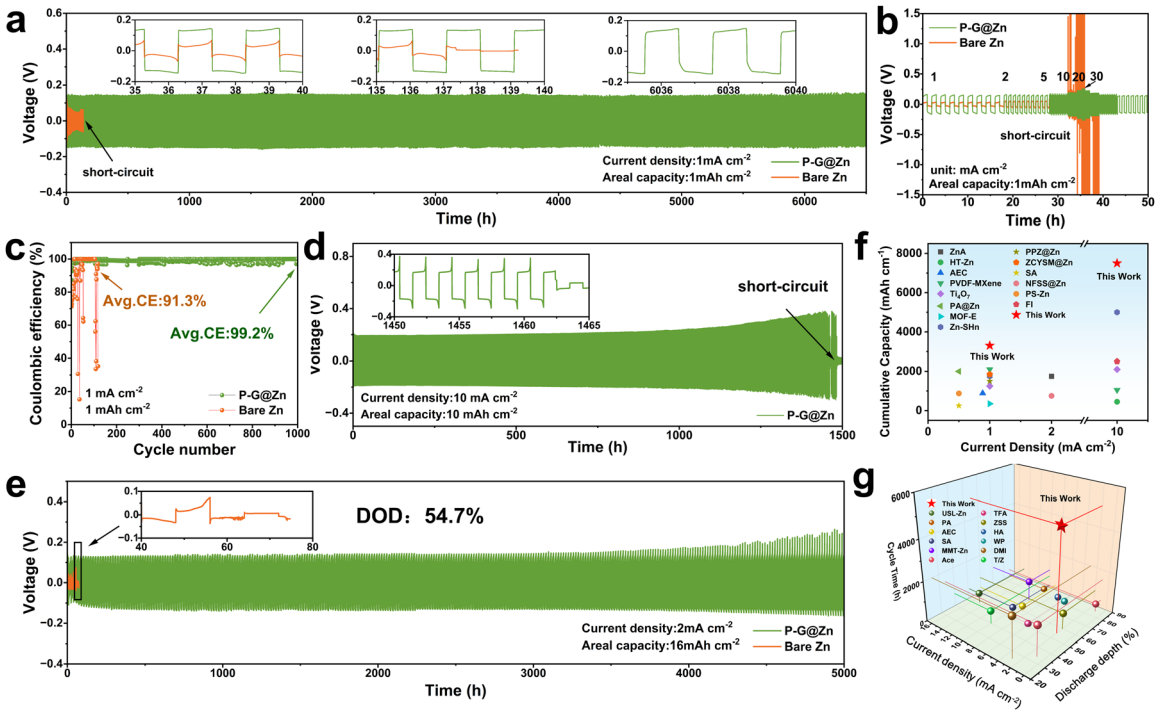

Fig. 5 Electrochemical stability and reversibility of Zn electrodes. (a) The long-term cycling performance of Zn||Zn symmetric cells at a current density of 1 mA cm^{-2} and an areal capacity of 1 mAh cm^{-2}. (b) Cycling performance of Zn||Zn symmetric cells at various current densities at 1 mAh cm^{-2}. (c) Coulombic efficiencies of Cu||Zn cells at a current density of 1 mA cm^{-2} and an areal capacity of 1 mAh cm^{-2}. (d) Cycling performance of P–G@Zn||P–G@Zn symmetric cells at current density of 10 mA cm^{-2} and areal capacity of 10 mAh cm^{-2}. (e) Cycling performance of Zn||Zn symmetric cells at the Zn DOD of 54.7%. (f) and (g) Comparison of the reversible electrochemical performance of this work with recent reports focusing on AZIBs.

zinc loss from uneven deposition/stripping, the HER and byproduct formation also consume zinc ions and contribute to reduced CE. As shown in Fig. 5c, the bare Cu||Zn cell exhibits only 160 cycles at a current density of 1 mA cm^{-2}, with significant fluctuations in CE. In contrast, the P–G@Cu||P–G@Zn cell achieves an average CE of 99.2% under the same conditions, maintaining a stable cycle life of 1000 cycles (Fig. S37). At higher current density and capacity (10 mA cm^{-2}, 10 mAh cm^{-2}), P–G@Zn demonstrates exceptional durability, achieving a cycle life of 1500 h (Fig. 5d).

To assess its practical potential, the Zn||Zn cell underwent a rigorous deep discharge test (Fig. 5e). The bare Zn||Zn cell deactivated after just four cycles (Fig. S38), whereas the P–G@Zn||P–G@Zn cell exhibited remarkable stability, sustaining a cycle life of 5000 h, which is approximately 78 times longer. Even under extreme discharge depths (DOD_{Zn} = 68.32% and 88.82%), P–G@Zn maintained cycling stability for over 700 and 500 h, respectively (Fig. S39 and S40). Performance comparison graphs (Fig. 5f and g) further highlight the superior cycling stability of P–G@Zn. Existing studies typically use zinc plates over 100-μm thick to enhance electrical stability.[19] However, limited zinc utilization remains a major obstacle to the widespread application of AZIBs. The P–G SEI layer significantly increases electrochemical stability and enables prolonged cycling under high discharge depths, outperforming similar studies. These results present a promising strategy for advancing the commercial viability of aqueous zinc batteries.

The practical application potential of P–G@Zn was further validated using two distinct cathodes: V_2O_5 and I_2. At a scan rate of 1 mV s^{-1}, the cyclic voltammogram profiles of the Zn||V_2O_5 cells manifested two pairs of redox peaks.[16,56] Critically, the P–G SEI layer, suppresses interfacial side reactions and facilitates Zn^{2+} transport, thereby optimizing ion migration dynamics, reducing the voltage gap between oxidation and reduction, and enhancing reaction reversibility (Fig. 6a). Coupled with the reduced impedance of the full cells protected by the coating, these findings verify that the P–G SEI layer promotes faster reaction kinetics and minimizes polarization in the Zn||V_2O_5 cell (Fig. S41 and S42).[57] Furthermore, as shown in Fig. 6b and Fig. S43, the cell demonstrates excellent rate performance at increasing current densities, exhibiting superior stability and high reversibility compared to bare Zn.[58] Remarkably, the P–G@Zn||V_2O_5 full cell retained 90% of its capacity after 2000 cycles at a current density of 2 A g^{-1},

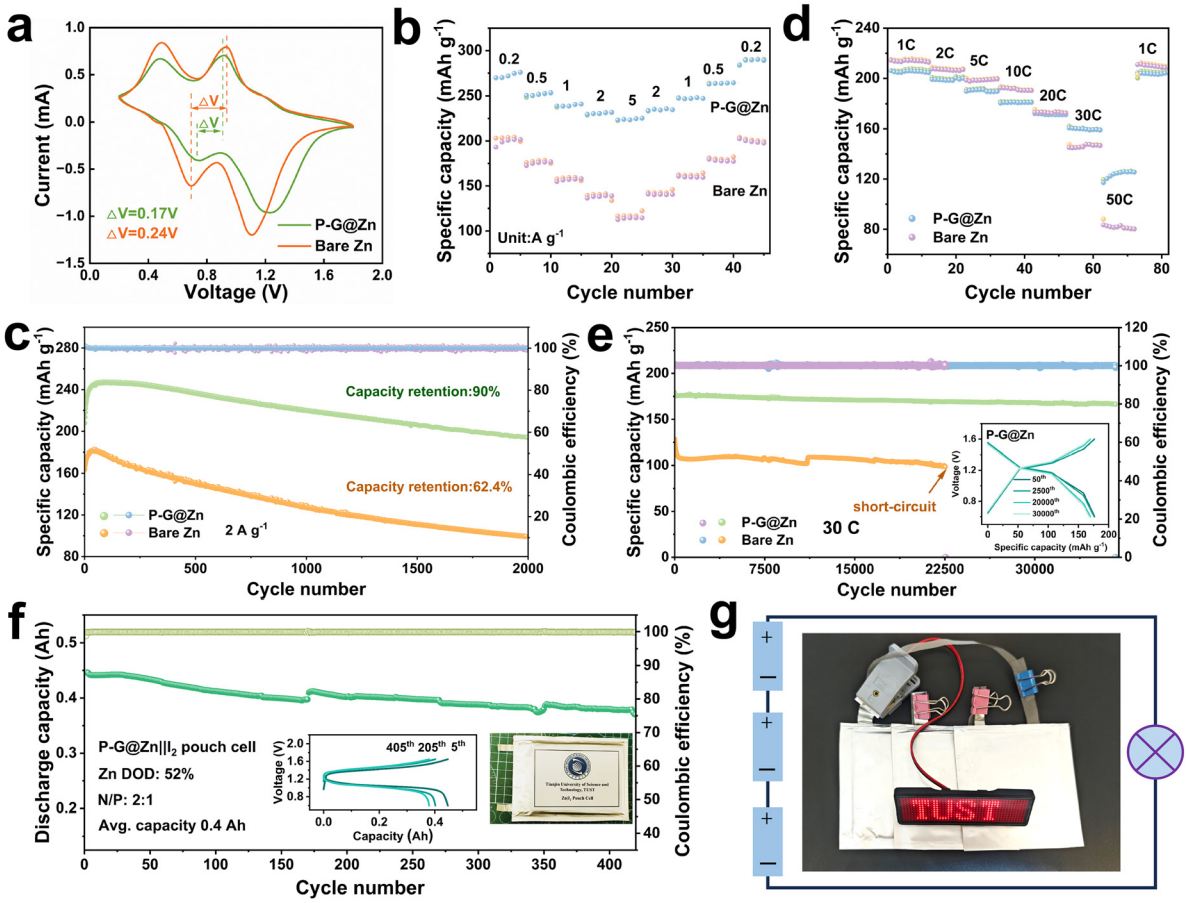

Fig. 6 Electrochemical behavior of Zn||V_2O_5 and Zn||I_2 full cells. (a) CV curves at a scan rate of 1 mV s^{-1} for Zn||V_2O_5 full cells. (b) Rate performance of Zn||V_2O_5 full cells. (c) Long-term cycling performances at current density of 2 A g^{-1}. (d) Rate performance of Zn||I_2 full cells. (e) Long-term cycling performances at current density of 30C. (f) Cycling performance of Zn||I_2 pouch cell at 1 A g^{-1}. (g) Optical image of typical electrical devices powered by Zn||I_2 pouch cells.

significantly outperforming the bare Zn||V_2O_5 cell, which retained only 62.4% (Fig. 6c).

Similarly, the P–G@Zn||I_2 full cell exhibited superior kinetics and stability. As shown in Fig. 6d, the slope of the fitted curve for the P–G@Zn redox peaks in the CV curves at various scan rates surpasses that of bare Zn (Fig. S44 and S45), indicating enhanced stability within the P–G SEI layer. This stability facilitates the fast migration of Zn^{2+} across the electrolyte and separator, thereby enabling exceptional electrochemical performance.[59–61] At a high current density of 30C, the P–G@Zn||I_2 full cell retained an impressive capacity of 175 mAh g^{-1} after 36 000 cycles (Fig. 6e). In contrast, the bare Zn||I_2 cell maintained only 98.2 mAh g^{-1} after 20 000 cycles, corresponding to a retention rate of 95.4% (Fig. S46).

To evaluate Zn||I_2 full-cell performance under practical conditions, we assembled soft-pack cells with high I_2 mass loading (15 mg cm^{-2}) using a P–G SEI layer fabricated *via* thermal spraying (Fig. S47 and S48).[62–64] Notably, the ability to controllably and uniformly form the SEI layer represents a major bottleneck for scaling up the thermal spraying process. The pouch cell, with an area of 8 × 9 cm^2 and tested at a Zn DOD of 52%, delivered a high specific capacity of 341.85 mAh g^{-1} with 82.8% capacity retention after 400 cycles at 1 A g^{-1} (Fig. 6f). Additionally, Fig. 6g depicts three small-sized P–G@Zn||I_2 pouch cells powering over 50 light-emitting diodes requiring a working voltage of 3–4 V. These findings underscore the efficacy of the P–G SEI layer in stabilizing Zn electrodes, reducing side reactions, and enhancing redox reversibility, thus offering a promising strategy for the development of high-performance aqueous zinc batteries (Fig. S49 and S50).

Conclusions

In this study, we introduced a hybrid SEI layer with an ion-pumping effect as an innovative solution to enhance the reversibility and stability of zinc anodes, and advance the practical application of aqueous zinc-ion batteries (AZIBs). The P–G SEI layer suppresses corrosion and hydrogen evolution reactions, while promoting uniform Zn^{2+} deposition, resulting in a remarkable electrochemical performance. With a high Zn^{2+} transference number of 0.77, fast desolvation kinetics, and exceptional cycling stability lasting over 6500 h in symmetrical cells and achieving ultra-long lifespans in full-cell configurations, the P–G SEI layer demonstrates outstanding durability. Beyond symmetrical cells, it enables robust cycling in Zn||V_2O_5 and Zn||I_2 systems, including 36 000 cycles with 95.5% retention in Zn||I_2 coin cells and excellent performance in practical Zn||I_2 pouch cells. These findings highlight the P–G SEI layer as a transformative design for optimizing zinc anodes and advancing next-generation energy storage technologies.

Author contributions

L. Y. conceived the idea. Y. S. and X. L. carried out the materials synthesis and electrochemical characterization. Q. M., Z. R., N. X., and K. L. provided important experimental insights. L. J., J. L., Y. K., and L. T. reviewed and edited the manuscript. A. Y. and B. C. supervised the experiments and revised the content. All the authors discussed the results and contributed to writing the manuscript.

Conflicts of interest

There are no conflicts to declare.

Data availability

The data that support the findings of this study are available from the corresponding author upon reasonable request.

Supplementary information is available. See DOI: **https://doi.org/10.1039/d5ee01408e**

Acknowledgements

This work was supported by the National Natural Science Foundation of China (22208117), and the fellowship of China Postdoctoral Science Foundation (2023M741818). The authors thank the synchrotron X-ray tomography measurement on the BMIT-BM beamline at the Canadian Light Source. The authors also acknowledge the XPS and TOF-SIMS characterizations at the Vacuum Interconnected Nanotech Workstation (Nano-X), and Suzhou Institute of Nano-Tech and Nano-Bionics, Chinese Academy of Sciences (Nano-X). The authors also thank the Analytic and Testing Center of Tianjin University of Science and Technology for the characterization, and Na Yang for the molecular dynamic simulation. Leixin Yang, Yujie Shen, and Xintao Long contributed equally to this work.

References

1 C. Zhu, P. Li, G. Xu, H. Cheng and G. Gao, *Coord. Chem. Rev.*, 2023, **485**, 215142.
2 Z. Peng, Z. Feng, X. Zhou, S. Li, X. Yin, Z. Zhang, N. Zhao, Z. He, L. Dai, L. Wang and C. Lu, *J. Energy Chem.*, 2024, **91**, 345–369.
3 Q. Zhao, T. Xu, K. Liu, H. Du, M. Zhang, Y. Wang, L. Yang, H. Zhang, X. Wang and C. Si, *Energy Storage Mater.*, 2024, **71**, 103605.
4 L. Tang, H. Peng, J. Kang, H. Chen, M. Zhang, Y. Liu, D. H. Kim, Y. Liu and Z. Lin, *Chem. Soc. Rev.*, 2024, **53**, 4877–4925.
5 X. Li, *Nat. Energy*, 2025, **10**, 670.
6 M. Wu, Y. Zhang, L. Xu, C. Yang, M. Hong, M. Cui, B. C. Clifford, S. He, S. Jing, Y. Yao and L. Hu, *Matter*, 2022, **5**, 3402–3416.
7 C. Wang, X. Zeng, J. Qu, J. M. Cairney, Q. Meng, P. J. Cullen and Z. Pei, *Matter*, 2023, **6**, 3993–4012.
8 H. Peng, Y. Fang, J. Wang, P. Ruan, Y. Tang, B. Lu, X. Cao, S. Liang and J. Zhou, *Matter*, 2022, **5**, 4363–4378.

9 S. Wang, J. Li, B. Yang, B. Zhang, Z. Zhang, S. Zhou, Q. Wang, J. Ma and Z. Jin, *Nano Lett.*, 2025, **25**, 5406–5414.
10 R. Zhao, J. Yang, X. Han, Y. Wang, Q. Ni, Z. Hu, C. Wu and Y. Bai, *Adv. Energy Mater.*, 2023, **13**, 2203542.
11 B. Ren, S. Hu, A. Chen, X. Zhang, H. Wei, J. Jiang, G. Chen, C. Zhi, H. Li and Z. Liu, *Adv. Energy Mater.*, 2024, **14**, 2302970.
12 R. Zhao, Y. Yang, G. Liu, R. Zhu, J. Huang, Z. Chen, Z. Gao, X. Chen and L. Qie, *Adv. Funct. Mater.*, 2021, **31**, 2001867.
13 K. Zhou, X. Yu, X. Dong, Z. Guo and Y. Wang, *Acc. Chem. Res.*, 2025, **58**, 599–611.
14 X. Cai, X. Wang, Z. Bie, Z. Jiao, Y. Li, W. Yan, H. J. Fan and W. Song, *Adv. Mater.*, 2024, **36**, 2306734.
15 Y. Song, Y. Liu, S. Luo, Y. Yang, F. Chen, M. Wang, L. Guo, S. Chen and Z. Wei, *Adv. Funct. Mater.*, 2024, **34**, 2316070.
16 X. Cai, W. Tian, Z. Zhang, Y. Sun, L. Yang, H. Mu, C. Lian and H. Qiu, *Adv. Mater.*, 2024, **36**, 2307727.
17 V. Aupama, J. Sangsawang, W. Kao-ian, S. Wannapaiboon, J. Pimoei, W. yoopensuk, M. Opchoei, Z. Tehrani, S. Margadonna and S. Kheawhom, *Electrochim. Acta*, 2024, **506**, 145059.
18 N. Yang, Y. Gao, F. Bu, Q. Cao, J. Yang, J. Cui, Y. Wang, J. Chen, X. Liu and C. Guan, *Adv. Mater.*, 2024, **36**, 2312934.
19 R. Yao, Y. Zhao, L. Wang, C. Xiao, F. Kang, C. Zhi and C. Yang, *Energy Environ. Sci.*, 2024, **17**, 3112–3122.
20 A. Sigel, H. Sigel and R. K. O. Sigel, The alkali metal ions: their role for life, *Metal Ions in Life Sciences*, Springer, 2019, vol. 16, pp. 485–556.
21 A. Xia, X. Pu, Y. Tao, H. Liu and Y. Wang, *Appl. Surf. Sci.*, 2019, **481**, 852–859.
22 J. G. Lyons, J. E. Kennedy, S. Lordan, L. M. Geever and C. L. Higginbotham, *J. Mater. Sci.*, 2010, **45**, 3204–3214.
23 T. González, R. Castro-Muñoz, M. Vera, G. Merlet, L. Pino-Soto and R. Cabezas, *J. Ind. Eng. Chem.*, 2024, **135**, 67–86.
24 Z. Zhou, Y. Zhang, P. Chen, Y. Wu, H. Yang, H. Ding, Y. Zhang, Z. Wang, X. Du and N. Liu, *Chem. Eng. Sci.*, 2019, **194**, 142–147.
25 B. Luo, Y. Wang, S. Zheng, L. Sun, G. Duan, J. Lu, J. Huang and Z. Ye, *Energy Storage Mater.*, 2022, **51**, 610–619.
26 J. Li, S. Zhou, X. Meng, Y. Chen, C. Fu, A. Azizi, X. Zhao, W. Xie, Z. Chang and A. Pan, *Sci. Bull.*, 2023, **68**, 1283–1294.
27 W. Shi, Z. Song, W. Zhang, S. Lian, F. Huang, Q. An and Q. Li, *Energy Environ. Sci.*, 2024, **17**, 7372–7381.
28 J. Wang, L. Jiao, Q. Liu, W. Xin, Y. Lei, T. Zhang, L. Yang, D. Shu, S. Yang, K. Li, C. Li, C. Yi, H. Bai, Y. Ma, H. Li, W. Zhang and B. Cheng, *J. Energy Chem.*, 2024, **94**, 10–18.
29 W. Zhang, M. Dong, K. Jiang, D. Yang, X. Tan, S. Zhai, R. Feng, N. Chen, G. King, H. Zhang, H. Zeng, H. Li, M. Antonietti and Z. Li, *Nat. Commun.*, 2022, **13**, 5348.
30 L. Yang, Q. Ma, Y. Yin, D. Luo, Y. Shen, H. Dou, N. Zhu, R. Feng, Y. Kong, A. Yu, B. Cheng, X. Wang and Z. Chen, *Nano Energy*, 2023, **117**, 108799.
31 Z. Zhao, J. Zhao, Z. Hu, J. Li, J. Li, Y. Zhang, C. Wang and G. Cui, *Energy Environ. Sci.*, 2019, **12**, 1938–1949.
32 K. Qiu, G. Ma, Y. Wang, M. Liu, M. Zhang, X. Li, X. Qu, W. Yuan, X. Nie and N. Zhang, *Adv. Funct. Mater.*, 2024, **34**, 2313358.
33 H. Du, R. Zhao, Y. Yang, Z. Liu, L. Qie and Y. Huang, *Angew. Chem., Int. Ed.*, 2022, **61**, e202114789.
34 Z. Shi, M. Li, X. Fu, Y. Zhang, S. Jiao and Y. Zhao, *Adv. Funct. Mater.*, 2024, **34**, 2316427.
35 C. Guo, J. Zhou, Y. Chen, H. Zhuang, J. Li, J. Huang, Y. Zhang, Y. Chen, S.-L. Li and Y.-Q. Lan, *Angew. Chem., Int. Ed.*, 2023, **62**, e202300125.
36 H. Dong, X. Hu, R. Liu, M. Ouyang, H. He, T. Wang, X. Gao, Y. Dai, W. Zhang, Y. Liu, Y. Zhou, D. J. L. Brett, I. P. Parkin, P. R. Shearing and G. He, *Angew. Chem., Int. Ed.*, 2023, **62**, e202311268.
37 M. Wu, X. Wang, F. Zhang, Q. Xiang, Y. Li and J. Guo, *Energy Environ. Sci.*, 2024, **17**, 619–629.
38 T. Long, Q.-Y. Zhao, G.-Y. Yin, P.-X. Xie, S. Liu, X. Ma, Q. Wu, B.-Y. Lu, Z. Dai and X.-X. Zeng, *Adv. Funct. Mater.*, 2024, **34**, 2315539.
39 W. Chen, Y. Tan, C. Guo, X. Zhang, X. He, W. Kuang, H. Weng, H. Du, D. Huang, Y. Huang, J. Xu and H. He, *J. Colloid Interface Sci.*, 2024, **669**, 104–116.
40 L. Yao, G. Wang, F. Zhang, X. Chi and Y. Liu, *Energy Environ. Sci.*, 2023, **16**, 4432–4441.
41 X. Wang, Y. Ying, X. Li, S. Chen, G. Gao, H. Huang and L. Ma, *Energy Environ. Sci.*, 2023, **16**, 4572–4583.
42 S. Huang, R. Tang, X. Liu, Y. Zhang, Y. Tang, Z. Wen, M. Ye, Y. Yang and C. C. Li, *Energy Environ. Sci.*, 2024, **17**, 591–601.
43 Z. Zheng, S. Guo, M. Yan, Y. Luo and F. Cao, *Adv. Mater.*, 2023, **35**, 2304667.
44 X. Wang, Y. Ying, X. Li, S. Chen, G. Gao, H. Huang and L. Ma, *Energy Environ. Sci.*, 2024, **17**, 3228–3229.
45 Z. Shi, M. Yang, Y. Ren, Y. Wang, J. Guo, J. Yin, F. Lai, W. Zhang, S. Chen, H. N. Alshareef and T. Liu, *ACS Nano*, 2023, **17**, 21893–21904.
46 C. Chang, S. Hu, T. Li, F. Zeng, D. Wang, S. Guo, M. Xu, G. Liang, Y. Tang, H. Li, C. Han and H.-M. Cheng, *Energy Environ. Sci.*, 2024, **17**, 680–694.
47 Z. Yang, F. Lai, Q. Mao, C. Liu, R. Wang, Z. Lu, T. Zhang and X. Liu, *Adv. Mater.*, 2024, **36**, 2311637.
48 X. Yang, Q. Zhou, S. Wei, X. Guo, P. J. Chimtali, W. Xu, S. Chen, Y. Cao, P. Zhang, K. Zhu, H. Shou, Y. Wang, X. Wu, C. Wang and L. Song, *Small Methods*, 2024, **8**, 2301115.
49 B. Liu, C. Wei, Z. Zhu, Y. Fang, Z. Bian, X. Lei, Y. Zhou, C. Tang, Y. Qian and G. Wang, *Angew. Chem., Int. Ed.*, 2022, **61**, e202212780.
50 Q. Zhang, Y. Ma, Y. Lu, Y. Ni, L. Lin, Z. Hao, Z. Yan, Q. Zhao and J. Chen, *J. Am. Chem. Soc.*, 2022, **144**, 18435–18443.
51 Q. Hu, J. Hou, Y. Liu, L. Li, Q. Ran, J. Mao, X. Liu, J. Zhao and H. Pang, *Adv. Mater.*, 2023, **35**, 2303336.
52 Y. Guo, W. Cai, Y. Lin, Y. Zhang, S. Luo, K. Huang, H. Wu and Y. Zhang, *Energy Storage Mater.*, 2022, **50**, 580–588.
53 J. Zhu, W. Deng, N. Yang, X. Xu, C. Huang, Y. Zhou, M. Zhang, X. Yuan, J. Hu, C. Li and R. Li, *Small*, 2022, **18**, 2202509.

54 R. Zhang, Y. Feng, Y. Ni, B. Zhong, M. Peng, T. Sun, S. Chen, H. Wang, Z. Tao and K. Zhang, *Angew. Chem., Int. Ed.*, 2023, **62**, e202304503.
55 J.-L. Yang, J. Li, J.-W. Zhao, K. Liu, P. Yang and H. J. Fan, *Adv. Mater.*, 2022, **34**, 2202382.
56 G. Zhu, H. Zhang, J. Lu, Y. Hou, P. Liu, S. Dong, H. Pang and Y. Zhang, *Adv. Funct. Mater.*, 2024, **34**, 2305550.
57 Z. Wang, X. Zhu, X. Tao, P. Feng, J. Wang and J. Chen, *Adv. Funct. Mater.*, 2024, **34**, 2316223.
58 J. Duan, J. Dong, R. Cao, H. Yang, K. Fang, Y. Liu, Z. Shen, F. Li, R. Liu, H. Li and C. Chen, *Adv. Sci.*, 2023, **10**, 2303343.
59 D. Dong, T. Wang, Y. Sun, J. Fan and Y.-C. Lu, *Nat. Sustainability*, 2023, **6**, 1474–1484.
60 S.-J. Zhang, J. Hao, H. Wu, C.-C. Kao, Q. Chen, C. Ye and S.-Z. Qiao, *ACS Nano*, 2024, **18**, 28557–28574.
61 L. Yang, D. Luo, Y. Zheng, T. Yang, Q. Ma, Y. Nie, H. Dou, Y. Zhang, R. Huang, A. Yu, L. Shui, X. Wang and Z. Chen, *Adv. Funct. Mater.*, 2022, **32**, 2204778.
62 X. Wang, J. Meng, X. Lin, Y. Yang, S. Zhou, Y. Wang and A. Pan, *Adv. Funct. Mater.*, 2021, **31**, 2106114.
63 S.-J. Zhang, J. Hao, H. Wu, Q. Chen, C. Ye and S.-Z. Qiao, *Adv. Mater.*, 2024, **36**, 2404011.
64 H. Wu, J. Hao, S. Zhang, Y. Jiang, Y. Zhu, J. Liu, K. Davey and S.-Z. Qiao, *J. Am. Chem. Soc.*, 2024, **146**, 16601–16608.

